

# Lawrence Berkeley National Laboratory

LBL Publications

## Title

Adsorption and Capillary Condensation-Induced Imbibition in Nanoporous Media

## Permalink

<https://escholarship.org/uc/item/0840736m>

## Journal

Langmuir, 35(29)

## ISSN

0743-7463

## Authors

Cihan, Abdullah

Tokunaga, Tetsu K

Birkholzer, Jens T

## Publication Date

2019-07-23

## DOI

10.1021/acs.langmuir.9b00813

Peer reviewed

# Adsorption and Capillary Condensation-Induced Imbibition in Nanoporous Media

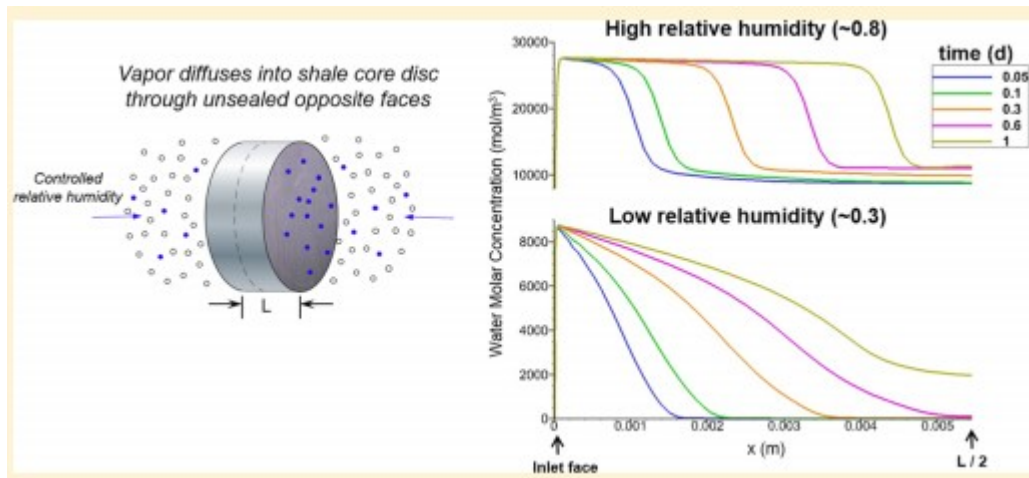
Abdullah Cihan,\* Tetsu K. Tokunaga, and Jens T. Birkholzer

Energy Geosciences Division, Lawrence Berkeley National Laboratory,  
Berkeley, California 94720, United States

\*E-mail: acihan@lbl.gov.

## Abstract

Multiphase flow phenomena in nanoporous media are encountered in many science and engineering applications. Shales, for example, possessing complex nanopore networks, have considerable importance as source rocks for unconventional oil and gas production and as low-permeability seals for geologic carbon sequestration or nuclear waste disposal. This study presents a theoretical investigation of the processes controlling adsorption, capillary condensation, and imbibition in such nanoporous media, with a particular focus on understanding the effects of fluid–fluid and fluid–pore wall interaction forces in the interconnected nanopore space. Building on a new theoretical framework, we developed a numerical model for the multiphase nanoporous flow and tested it against water vapor uptake measurements conducted on a shale core sample. The model, which is based on the density functional approach, explicitly includes the relevant interaction forces among fluids and solids while allowing for a continuum representation of the porous medium. The experimental data include gravimetrically measured mass changes in an initially dry core sample exposed to varying levels of relative humidity, starting with a low relative humidity ( $rh = 0.31$ ) followed by a period of a higher relative humidity ( $rh = 0.81$ ). During this process, water vapor uptake in the dry core is recorded as a function of time. Our model suggests that, under low  $rh$  conditions, the flow within the shale sample is controlled by adsorption- and diffusion-type processes. After increasing the  $rh$  to 0.81, the uptake of water vapor becomes more significant, and according to our model, this can be explained by capillary condensation followed by immiscible displacement in the core sample. It appears that strong fluid–pore wall attractive forces cause condensation near the inlet, which then induces water imbibition further into sample.



## Introduction

Multiphase fluid behavior in nanoporous materials is of interest for various science and engineering applications, including geoscience applications, (1–3) chemical and material engineering, (4,5) and biological sciences. (6,7) In the context of geoscience applications, shales and mudstones are commonly occurring sedimentary rocks that have considerable importance as low-permeability seals for geologic carbon sequestration and nuclear waste disposal or, with increasing emphasis over the last two decades, as large reserves for unconventional oil and gas production. Pores within these rocks are predominantly in the micropore (<2 nm) and mesopore (2 to 50 nm) size categories. (8,9) When the pore sizes approach nanoscales, physicochemical interactions among fluid and solid molecules can alter bulk fluid phase properties such as phase composition, density, viscosity, and interfacial tension. (10–12) Likewise, basic macroscopic transport properties in porous media such as permeability and diffusivity can become strongly influenced by fluid–pore wall interactions in addition to the effects of pore size distribution and connectivity. (13–15)

Understanding the collective behavior of fluid–fluid and fluid–pore wall interaction forces in interconnected nanopore spaces is critical for solving various subsurface energy challenges. Water imbibition during hydraulic fracturing for hydrocarbon production can result in pore blocking near the fracture–rock matrix zones due to strong attraction of water to the rock matrix and reduce the hydrocarbon recovery from unconventional reservoirs. (9,16) Shale gas reservoirs may contain a significant amount of hydrocarbon condensates, in addition to adsorbed gas and free gas. (10) The hydrocarbon condensates may form in nanopores of organic matter in shale gas reservoirs. (15) Accounting for capillary condensation can considerably change the estimated hydrocarbon storage due to increased density (17) and can also have an impact on production from these reservoirs, but the effects of capillary condensation are currently not well understood. (10)

Recent experimental studies show that a liquid phase can form in nanopores from a vapor phase at relative humidity (rh) conditions well below the vapor saturation values.(18) As idealized nanoporous medium samples were exposed to vapor at their boundaries, a liquid-like fluid formed at the vicinity of the inlet and subsequently filled the nanopores in an imbibition-like manner.(18,19) Similar experiments were conducted with shale rock samples containing complex nanoscale pore networks.(9,20) When exposed to low relative humidities ( $rh \approx 0.3$ ), water vapor uptake in these samples was found to be diffusion- and adsorption-controlled.(9) In contrast, tests conducted at higher rh (0.8) showed a more significant water uptake, and the measured mass increase of the samples implied occupation of the shale pores with capillary-condensed dense water. Unfortunately, a more detailed picture of the flow processes within these samples was not obtained as measuring the spatial properties in nanoporous media currently is very challenging(18,19) especially in partially hydrated natural media.(21) While experimental methods are still evolving to resolve the spatial behavior of fluids in nanoporous media,(22,23) a combination of new theoretical and experimental approaches is needed to better understand flow processes in complex nanoporous materials such as shales.

In this study, we employ a new continuum model for the nanoporous flow together with water vapor uptake data from shale experiments to explore processes and forces controlling adsorption, capillary condensation, and imbibition in nanoporous media. The new model is based on the density functional approach and includes interaction forces among fluids and solids at continuum scales of nanoporous materials.

## Theory

We present here a new mathematical model for a continuum representation of a multiphase multicomponent flow in nanoporous media. The starting point in the derivation is to define the free energy of the multiphase mixture in porous media as the density functional depending on molar concentrations. The theoretical developments below are given for isothermal conditions.

Description of the free energy density function as a function of molar densities has a long history.(24–28) Based on a generalization for multicomponent systems and a square-gradient approximation,(29) recent specific applications for a multiphase flow at a pore-scale include imbibition, drainage, capillary condensation, and adsorption along the pore walls. (30–32) Continuum-scale models based on similar approaches such as the phase-field method and diffuse interface approaches were also proposed for modeling gravity fingers during water infiltration in soil(33) and modeling the multiphase hydrocarbon flow in porous media.(34) Different from phase-field modeling approaches, density functional or diffuse interface approaches do not require a phase-field order parameter and thus are more convenient for application for multicomponent transport problems.

Here, we present an extended application of the classical density functional theory to represent the multiphase multicomponent flow in macroscopic nanoporous media where strong fluid–solid forces need to be accounted for. The Helmholtz free energy of an inhomogeneous system  $E_H$  at a constant temperature can be expressed as

$$E_H = \int_V \psi \, dV \quad (1)$$

where  $\psi$  is the local energy density defined as the free energy per unit volume  $V$  of a rigid porous medium. Considering the external potentials including the gravitational potential and the interaction potential of the solids acting on a  $N$ -component fluid mixture in a porous medium, the Helmholtz free energy density based on the square-gradient approximation can be expressed as

$$\psi = \psi_0(c_1, c_2, \dots, c_N) + \frac{\kappa_{ij}}{2} \nabla^2 c_i \nabla^2 c_j + \rho \phi_g + \sum_i \phi_{s,i} \quad (2)$$

where  $\psi_0(c_1, c_2, \dots, c_N)$  is the homogeneous Helmholtz free energy density defined in terms of energy per unit volume of void space,  $\phi$  is the porosity, and  $c_1, c_2, \dots, c_N$  are the molar concentrations of the components. The second term on the right-hand side of eq 2 represents the macroscopic fluid–fluid interfacial energy, and the coefficients ( $\kappa_{ij}$ ) are related to the correlation functions for molecular densities(27,35) in pore space. The last two terms of  $\psi$  include the external potential energy functions due to gravitational attraction,  $\phi_g$  (energy/mass), and fluid–solid interaction potentials for each component,  $\phi_{s,i}$  (energy/mole).  $\rho$  is the mixture density equal to  $\sum_i = 1^N c_i M_i$  where  $M_i$  is the molecular mass of the  $i$ th component.

The fluid–solid interactions contain individual continuum-scale interaction potentials  $\phi_{s,i}$  between the solid phase and the  $i$ th fluid component. The fluid–solid interaction forces, also known as surface forces (e.g., van der Waals, electrostatic, and structural forces),(36,37) result from electrostatic and electromagnetic fields generated by charges and oscillating molecular dipoles.  $\phi_{s,i}$  values can be functions of molar concentrations,  $\phi_{s,i}(c_1, c_2, \dots, c_N)$ , and can vary with space. The continuum-scale interaction potentials,  $\phi_{s,i}$ , are expected to be functions of intermolecular forces between solid molecules and fluid molecules and void and solid spatial distributions.

Based on the description of the free energy density in eq 2, we first obtain chemical potential and stress tensor expressions that drive the flow of multiphase mixtures to equilibrium in porous media. Then, continuity and momentum balance equations for the multiphase mixture are obtained. Detailed derivations of the chemical potential, stress tensor, and balance equations for a multicomponent system in porous media are presented in the Supporting Information (Section 1). The key equations are presented below. The chemical potential,  $\Phi_i$ , for the  $i$ th component is equal to the variational derivative of  $E_H$  with respect to  $c_i$  and expressed as

$$\sigma = -p_0 \mathbf{I} - \sum_i c_i \nabla \psi_0 + \sum_i \kappa_{ij} \nabla c_i \nabla c_j \quad (3)$$

Following Yang et al.,(35) based on a statement of mechanical equilibrium, we use eq 3 to obtain the static stress tensor expression as described in the Supporting Information. Then, through the stress tensor, we describe a momentum balance equation for a multiphase mixture. Neglecting the inertial forces in porous media, the momentum equation for the multiphase mixture can be expressed as

$$\nabla \cdot \mathbf{q} = -\nabla p + \nabla \cdot (\mathbf{k} \cdot \nabla p) + \nabla \cdot (\mu \nabla \mathbf{q}) \quad (4)$$

where  $\mathbf{q}$  is the specific discharge or Darcy velocity vector of the multiphase fluid mixture,  $\mathbf{k}$  is the permeability tensor,  $p$  is the thermodynamic pressure ( $p = -\psi_0 + \sum_i c_i \partial \psi_0 / \partial c_i$ ), and  $\mu$  is the effective viscosity of the multiphase mixture.

The first three terms in eq 4 resemble the classical Darcy equation for a single-phase flow. However, the proposed new representation of the momentum balance is different from the classical multiphase extension of the Darcy equation. Equation 4 does not include the relative permeability for different phases nor does it utilize a macroscopic capillary pressure-saturation function. Instead, the last two terms in eq 4 explicitly account for the effects of multiphase interfacial fluid-fluid and fluid-solid interaction forces.

The theoretical model described here and in the Supporting Information (Section 1) requires measurements or characterization of the transport parameters and constitutive models for continuum-scale description of fluid-solid interaction potentials,  $\psi_{s,i}$ , in porous media. The transport parameters include the effective viscosity of the mixture, permeability and porosity of the porous medium, effective diffusion coefficients, and values of the  $\kappa_{ij}$  coefficients in macroscopic porous media. In addition, the homogeneous Helmholtz free energy density,  $\psi_0$ , needs to be specified based on the equation of state for the multiphase mixture.

The fluid-fluid interfacial interaction term in eq 4 includes a third-order gradient of molar concentrations. The coefficients,  $\kappa_{ij}$ , are functions of interfacial tension for nonporous media.(38) In addition, for continuum-scale porous media systems,  $\kappa_{ij}$  is a function of void space properties, including pore size distribution and connectivity. Values of  $\kappa_{ij}$  control the macroscopic interfacial tension that changes with the thickness of the interfacial zone between the fluids. As a result, in numerical modeling studies,  $\kappa_{ij}$  is also a computational parameter that varies with the model resolution.(32) For instance, when carrying out calculations at higher model resolutions for the

same set of parameters,  $\kappa_{ij}$  values given at a lower model resolution must be scaled down by the square of the ratio of the grid sizes to obtain an equivalent solution with equivalent values of macroscopic interfacial tension. For a two-phase system under isothermal conditions, it can be assumed that  $\kappa_{ij} = \kappa$ .(29)

### Balance Equations for the Two-Phase, Two-Component System

For isothermal systems, the continuity equations for the molar concentration of the water-air two-phase mixture can be simplified as

$$\nabla \cdot (\mathbf{q} - \mathbf{J}_w - \mathbf{J}_a) = 0 \quad (5)$$

Neglecting the inertial forces, the momentum equation for the two-phase mixture becomes

$$0 = -\frac{\mu \mathbf{q}}{k} - \nabla p - \rho \nabla \phi + \phi \kappa (c_w + c_a) \nabla (\nabla^2 c_w + \nabla^2 c_a) - c_w \nabla \phi_{s,w}^* - c_a \nabla \phi_{s,a}^* \quad (6)$$

where the effective viscosity of the multiphase fluid,  $\mu$ , is represented using an interpolation procedure as a function of individual phase viscosity values and molar concentrations.(29) Employing the Maxwell-Stefan diffusion approach,(39) including Knudsen or matrix diffusivity contributions in low-permeability media, the diffusive fluxes are obtained from the following two equations for two components

$$\begin{aligned} -\frac{c_w}{RT} \nabla \Phi_w &= \frac{c_a \mathbf{J}_w - c_w \mathbf{J}_a}{c_t D_{aw} \tau} + \frac{\mathbf{J}_w}{D_{wM}} \\ -\frac{c_a}{RT} \nabla \Phi_a &= \frac{c_w \mathbf{J}_a - c_a \mathbf{J}_w}{c_t D_{aw} \tau} + \frac{\mathbf{J}_a}{D_{aM}} \quad (7) \end{aligned}$$

where  $\mathbf{J}_i$  is the diffusive flux vector for the  $i$ th component,  $c_t$  is the total molar concentration,  $R$  is the ideal gas constant,  $T$  is temperature,  $D_{aw}$  is the binary diffusion coefficient,  $D_{wM}$  is the effective matrix diffusion coefficient for water, and  $D_{aM}$  is the effective matrix diffusion coefficient for air.  $\tau$  is the tortuosity coefficient that is assumed to be a function of porosity as  $\tau = \phi^m$  where  $m$  is an empirical constant.

The effective binary diffusion coefficients and matrix diffusivities under multiphase flow conditions for each component are computed using an interpolation of the diffusion coefficients measured in liquid and gas phases. Following Vignes' approach,(40,41) the effective binary molecular diffusion coefficient is estimated as  $D_{aw} = D_{aw(l)}^{x_w} \times D_{aw(g)}^{1-x_w}$  where  $x_w$  is the mole fraction of water and  $D_{aw(l)}$  and  $D_{aw(g)}$  are the binary diffusion coefficients measured under equilibrium composition conditions in liquid and gas phases, respectively (Table1).  $D_{wM}$  and  $D_{aM}$  are approximated using the same interpolation approach as  $D_{wM} = D_{wM(l)}^{x_w} \times D_{wM(g)}^{1-x_w}$  and  $D_{aM} = D_{aM(l)}^{x_w} \times D_{aM(g)}^{1-x_w}$ .

**Table 1. Measured or Calculated Model Input Parameters  
( $T = 50\text{ }^{\circ}\text{C}$ )**

$\phi$ (–)	0.098
$\mu_w$ (Pa·s)	$5.50 \times 10^{-4}$
$\mu_a$ (Pa·s)	$1.96 \times 10^{-5}$
$D_{aw(l)}$ ( $\text{m}^2/\text{s}$ )	$4.90 \times 10^{-943}$
$D_{aw(g)}$ ( $\text{m}^2/\text{s}$ )	$2.97 \times 10^{-5}$
$c_{wl}$ ( $\text{mol}/\text{m}^3$ )	54888.17
$c_{wg}$ ( $\text{mol}/\text{m}^3$ )	4.59
$c_{al}$ ( $\text{mol}/\text{m}^3$ )	$4.87 \times 10^{-1}$
$c_{ag}$ ( $\text{mol}/\text{m}^3$ )	31.51
$f_{l1}$ ( $\text{Pa}\cdot\text{m}^6/\text{mol}^2$ )	$7.51 \times 10^{-1}$
$f_{l2}$ ( $\text{Pa}\cdot\text{m}^6/\text{mol}^2$ )	55.8
$f_{g1}$ ( $\text{Pa}\cdot\text{m}^6/\text{mol}^2$ )	3.57
$f_{g2}$ ( $\text{Pa}\cdot\text{m}^6/\text{mol}^2$ )	94.1

#### Representation of Homogeneous Energy Density

To represent the homogeneous Helmholtz free energy density, a quadratic equation similar to the one proposed by Armstrong et al.(30) was employed under fixed temperature conditions. Selection of this type of equation simplifies the numerical computations of the model. More realistic equations of state could be used to represent the energy density more accurately for more complicated mixtures.(42) Ignoring zeroth and first order terms as they vanish from hydrodynamic equations,(30) the homogeneous energy density functions for liquid and gas phases can be represented as

$$\psi_0 = f_l c_w^2 + f_l c_a^2 + f_g c_w^2 + f_g c_a^2 \quad (8)$$


where  $c_{wk}$  and  $c_{ak}$  are the equilibrium concentrations of the components in phase  $k$  (liquid or gas) at a fixed  $T$ . The parameters of the energy density functions ( $f_{l1}$ ,  $f_{l2}$ ,  $f_{g1}$ , and  $f_{g2}$ ) are obtained by fitting of the bulk moduli calculated based on eq 8 to compressibility data from equation of state properties for the air-water mixture, separately under liquid and gas conditions. The bulk modulus for homogeneous fluid phases can be obtained through  $K_k = \sum_{i=w,a} c_i \partial p_k / \partial c_i$  ( $k = l, g$ ) where  $p_k = -f_k + \sum_{i=w,a} c_i \partial f_k / \partial c_i$ . Given eq 8, the bulk moduli for liquid and gas phases can be represented as  $K_l = f_{l1} c_w^2 + f_{l2} c_a^2$  and  $K_g = f_{g1} c_w^2 + f_{g2} c_a^2$ , respectively. The bulk homogeneous energy density for the air-water mixture under two-phase conditions is expressed using an interpolation of  $f_l$  and  $f_g$  as  $\psi_0 = f_l f_g / (f_l + f_g) - P_{\text{ref}}$  where  $P_{\text{ref}}$  is the reference pressure for the equilibrium concentrations. In this study, equilibrium concentrations and the effective bulk modulus of the air-water



mixture in the liquid phase were calculated using an equation of state for liquid water. The dissolved air concentration in liquid water was estimated using Henry's law for pressure (atmospheric) and temperature (50 °C) conditions during the water vapor uptake experiment. For estimating the energy density parameters for humid air, ideal gas was employed. Table 1 lists some of the parameters used in the model. The rest of the model parameters are described below.

### Characterization of Fluid-Pore Wall Interaction Energy Potentials

Many molecular-dynamics studies exist to evaluate adsorption and condensation driven by vapor diffusion into individual pores.<sup>(44,45)</sup> Instead of a comprehensive molecular-level study, a more simplistic approach is followed here to assess qualitatively the fluid-solid interaction energy as a function of the mole fraction of fluids interacting with pore walls. We employ the many-body dissipative particle dynamics (MDPD) approach to compute for the water-pore wall interaction energy under different mole fractions in a cylindrical nanopore. The details of the MDPD simulations including the formulation and simulation parameters are presented in the Supporting Information (Section 2). Based on our analyses in the Supporting Information, we express the fluid-solid interaction energy functions in the numerical model (eq 5-7) for both water and air molecules in terms of energy per mole as


$$\text{[Redacted Equation]}$$
(9)

which represents the MDPD results reasonably well for the interaction energy of a water-pore wall system in a cylindrical nanopore.  $A_h$ ,  $\alpha$ , and  $\beta$  are empirical parameters that may vary depending on the pore geometry, pore size distribution, fluid, and solid-molecule types. The magnitudes and signs of the parameters may vary depending on the wettability of fluids. We estimate these parameters for the actual test sample based on the experimental data (Table 2). However, more detailed pore scale simulations considering pore connectivity and heterogeneity in pore sizes and solid material properties are needed for better description of fluid-solid interaction energy functions, but this is outside the scope of this study.

**Table 2. Estimated Model Parameters for a Marcellus Shale Sample**

$k_0$ (m <sup>2</sup> )	$1.45 \times 10^{-22}$
$\lambda$ (-)	1.91
$m$ (-), ( $\tau = \phi^m$ )	3.27
$\kappa$ (J·m <sup>2</sup> /mol <sup>2</sup> )	$1.21 \times 10^{-7} \times (\Delta x/109 \mu\text{m})^2$
$A_{fw}$ (J/mol)	$-1.62 \times 10^5$
$\alpha_w$ (m <sup>3</sup> /mol)	$7.75 \times 10^{-6}$
$\beta_w$ (m <sup>6</sup> /mol <sup>2</sup> )	$7.62 \times 10^{-10}$
$D_{wM(l)}$ (m <sup>2</sup> /s)	$3.10 \times 10^{-13}$
$D_{wM(g)}$ (m <sup>2</sup> /s)	$3.91 \times 10^{-8}$
$A_{fa}$ (J/mol)	$7.39 \times 10^1$
$\alpha_a$ (m <sup>3</sup> /mol)	$-3.34 \times 10^{-5}$
$D_{aM(l)}$ (m <sup>2</sup> /s)	$2.57 \times 10^{-12}$
$D_{aM(g)}$ (m <sup>2</sup> /s)	$7.84 \times 10^{-8}$
$\varphi_{sw}^*$ (J/mol) at inlet boundary (rh = 0.31)	$-4.47 \times 10^4$
$\varphi_{sw}^*$ (J/mol) at inlet boundary (rh = 0.81)	$-2.92 \times 10^3$

## Methods

### Experimental Data

Our theoretical analyses of capillary condensation use an experimental data set generated from water vapor uptake experiments in a core plug of a Marcellus shale rock. The porosity of the rock is 0.098, and the bulk density is approximately 2440 kg/m<sup>3</sup>. The same experimental procedure given by Tokunaga et al.(9) was used to gather data by gravimetrically measuring water vapor uptake as a function of time. The rh conditions used in the experiments are 0.31 and 0.81, both at 50 °C, in order to determine the impact of different levels of pore filling by adsorption and capillary condensation. Although pore size distributions were not measured on our sample, other studies have reported a predominance of 10 to 40 nm of effective diameter pores in Marcellus Shales.(46,47) For comparison, acknowledging the limitations of estimating pore radii with the Kelvin equation (eq 8), the Kelvin pore diameters associated with capillary condensation at our experimental temperature (50 °C) are 1.6 and 8.8 nm for rh = 0.31 and 0.81, respectively.

The sequence of sample preparation and testing is illustrated in Figure 1. The lateral walls of the shale core disc were sealed with epoxy and aluminum foil to allow vapor entry only at the exposed edges of the bedding planes (diffusion parallel to bedding planes). The length of the test sample ( $L$ ) is 1.09 cm, and the area of each exposed face is 4.3 cm<sup>2</sup>. The laterally sealed oven-dried sample was placed into an rh = 0.31 chamber, and water vapor

uptake was monitored for about 22 days. Then, the sample was transferred into an  $rh = 0.81$  chamber, and monitoring of water vapor continued for an additional 50 days. The  $rh = 0.31$  and  $0.81$  conditions were controlled with reservoirs of saturated aqueous  $MgCl_2$  and  $KCl$  solutions, respectively,(48) contained in an incubator kept at  $50 \pm 0.5$  °C.

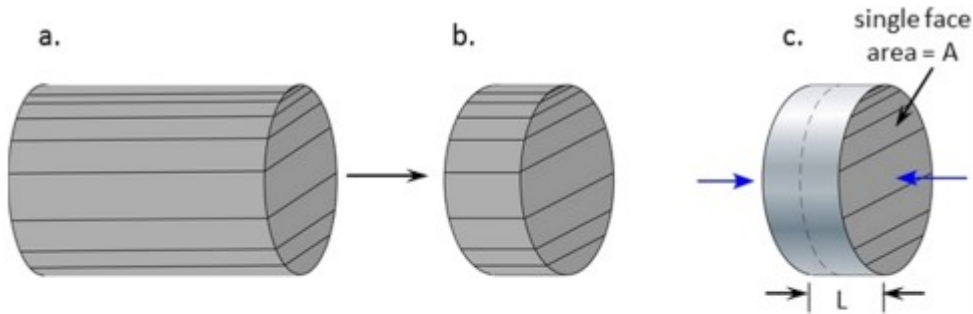


**Figure 1.** Sequence of preparing sidewall core plugs for measurements of water vapor diffusion/adsorption. (a) Sidewall core plug showing bedding planes along the original core axis. (b) Sliced core disc. (c) Core-disc sides sealed to allow vapor diffusion, entering from unsealed opposite faces.  $L = 1.09$  cm and  $A = 4.3$  cm<sup>2</sup>.

### Numerical Model

An in-house computer model was employed to numerically solve the coupled fourth-order partial differential equations in eq 5 for a two-component, two-phase fluid system based on the finite volume method. The water uptake experiment was simulated using a one-dimensional version of the numerical model, neglecting the effects of gravitational forces. Using the symmetrical configuration of the core, half of the domain was simulated from one of the inlet faces ( $x = 0$ ) to the center of the core ( $x = L/2$ ). The numerical model domain was discretized using a uniform grid size of  $109 \mu\text{m}$  in the  $x$  direction. Cutting the grid size by half results in negligible changes in the calculated water uptake as a function of time as long as the term  $\kappa$  is scaled properly with the grid size, as explained in the next section. However, to represent the sharp concentration changes near the inlet boundary, we reduced the grid sizes near the inlet where the sizes of the first 10 grid blocks varied between  $10.9$  and  $109 \mu\text{m}$ . Our selection of the grid size is to some extent consistent with the estimated representative sizes to represent a continuum scale of a shale rock matrix. Some of the earlier studies(49–51) have shown that the representative sizes of the shale rocks can vary between tens and a few hundreds of micrometers, depending on the shale type and the analyzed property (e.g., mineral content, porosity, and permeability).

Consistent with the experiment, dry air was assumed to initially occupy the shale pores. The subsequent  $rh$  increases were created in the model by

fixing the molar concentrations of air and water vapor at the inlet, representative of rh values changing to 0.31 and later to 0.81. The chemical potentials at the inlet boundary are functions of the derivative of the homogeneous Helmholtz free energy with respect to molar concentration and the fluid–solid (pore wall) interaction energy in different rh conditions, and their gradients drive the vapor transport into the core. The strengths of the fluid–solid interaction term,  $\phi_s^*$ , at  $rh = 0.31$  and  $rh = 0.81$  were fixed at the inlet boundary, and their values were estimated using the experimental data. Inside the model domain, eq 9 represented the fluid–solid interaction energies with the parameters ( $\alpha$  and  $\beta$ ) that are assumed to be independent of rh.

In nanoporous media, permeability can be a function of fluid–pore wall interactions as well as pore space properties.(13) The ratio of viscosity to permeability,  $\mu/k$ , in eq 6 represents an effective viscous resistance coefficient for the multicomponent multiphase fluid mixture. The pore scale MDPD modeling shows that the strength of the fluid–pore wall attraction energy increases with decreasing molar concentration of water. Because of the microscopic effects of the fluid–pore wall attractions, the effective permeability and  $\mu/k$  can be a complex function of fluid compositions. As stated earlier, we represent  $\mu$  using an interpolation procedure as a function of individual phase viscosity values and molar concentrations.(29) However, we neglected the additional potential effects of microscopic fluid–pore wall interactions on the individual phase viscosity(12) due to lack of information on the phase viscosities at macroscopic nanoporous media. Instead, to represent the effects of the fluid composition dependency and fluid–pore wall attractions on the effective viscous resistance, we used a simple permeability relationship such as  $k = k_a x_a + k_w x_w (c_w/c_{wl})^\lambda$  where  $\lambda$  is an empirical parameter that is  $\geq 0$ . As explained in the following section, the selected form of the permeability appears suitable to represent the fluid uptake data under both low and high rh conditions. We further assumed in this study that  $k_0 = k_a = k_w$  to reduce the number of unknown values. The parameters of the permeability model ( $k_0$  and  $\lambda$ ) are estimated inversely based on the experimental data.

Properties of shale can be very heterogeneous spatially even at a scale as small as the core plug used in the experiments.(8,9) Because the detailed knowledge of pore–solid spatial properties in the core is not available, the properties of the modeled shale core–fluid system are represented by equivalent homogeneous parameters. The objective of this work is to gain a general insight on processes affecting capillary condensation and imbibition in nanoporous media rather than to simulate the exact properties of the shale core.

## Results and Discussion

### Measured Water Uptake

A time-dependent record of normalized water mass in Figure 2 shows that the water vapor uptake is initially quite rapid before leveling out for both cases of  $rh = 0.31$  and  $0.81$  (roughly proportional to the square root of time). However, the data indicate a much greater water vapor uptake at higher  $rh$ . The significant mass changes observed in the experiment are an indication of liquid water formation by condensation in the rock pore space. Unfortunately, spatial measurements of fluid component concentrations were not available in this study. At  $rh = 0.31$ , the initially fast uptake continued for about 3 days, and the mass of water uptake appeared to reach equilibrium at about 8 days. The period of fast water uptake was shorter at  $rh = 0.81$ , but the mass continued to increase very slowly during the additional 50-day period.

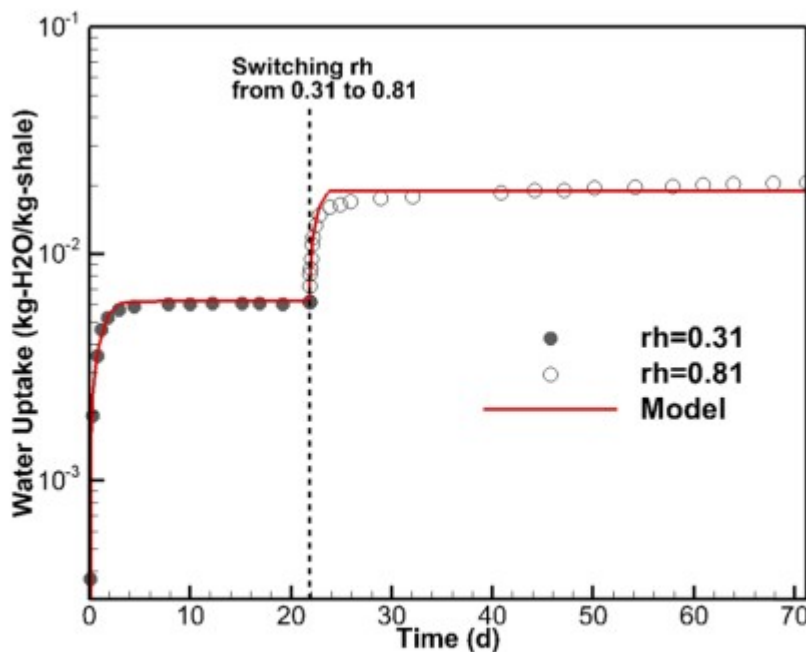


**Figure 2.** Comparisons of the model estimated and the measured water uptake in the Marcellus shale rock core.

### Model Results and Sensitivity Analysis

Overall, the model appears to represent the water mass changes reasonably well, except for the continued slow mass increases over long time periods in the  $rh = 0.81$  data (Figure 2). The slow mass increase could be indicative of chemical interactions between water and the rock over longer times (e.g., pyrite oxidation and clay swelling),(52,53) which are outside the scope of this study.

Table 2 lists the estimated 15 parameters for the shale rock core with water and air fluid components. The parameters were estimated inversely using the differential evolution algorithm.(54) The differential evolution (DE), a derivative-free global optimization algorithm, has been successfully used to

find optimal solutions that involve a large number of unknown parameters in our earlier studies(55,56) as in this study. Although the DE is a powerful evolutionary algorithm, it may not always guarantee unique solutions. DE applies stochastic search algorithms within predefined ranges of parameter space. Proper initialization of the parameter bounds is necessary for the optimization algorithm to converge to physically consistent parameter values. We constrained possible ranges of some parameters such as permeability and diffusion coefficients for shales based on the limited data in the literature. However, our model also includes new parameters such as fluid–fluid and fluid–pore wall interaction functions, and for the less known parameters, we start the DE optimization algorithm with wide parameter bounds to assure that unknown optimal values of the parameters do not fall beyond the search space.

After obtaining the optimal set of parameters based on the DE algorithm, we conducted a local sensitivity analysis to obtain insights on the effects of parameter uncertainty on the model results. Table3 lists the overall parameter sensitivities under different rh conditions. Normalized sensitivity coefficients were calculated based on evaluating the partial derivative of modeled fluid uptake with respect to each selected parameter as  $p_{i\text{best}}/U_{\text{best}}(t) \partial U / \partial p_i$  where  $U$  is the water uptake (mass/mass),  $p_i$  is the  $i$ th parameter value, and the subscript “best” indicates the optimal or base parameter values. We changed the logarithm of the base parameter values by  $\pm 10\%$  for calculating the derivatives; except for  $\lambda$ , we perturbed its absolute value by  $\pm 10\%$ . Discrete values of the calculated sensitivity coefficients as a function of time are summed over the total durations of the different rh conditions. The tabulated sensitivity values in Table3, in decreasing order, represent the summed contribution of each parameter to the model output relative to the contributions of the other parameters.

**Table 3. Results of the Local Sensitivity Analysis<sup>a</sup>**

no.	rh = 0.31		rh = 0.81	
	parameter	sensitivity	parameter	sensitivity
1	$A_{hw}$	14.69	$A_{hw}$	5.90
2	$\varphi_{sw}^*$ at boundary	10.37	$\kappa$	3.97
3	$\kappa$	6.82	$\varphi_{sw}^*$ at boundary	1.60
4	$\lambda$	1.66	$\alpha_w$	1.00
5	$\alpha_w$	1.09	$\lambda$	0.49
6	$D_{aw(g)}$	0.31	$D_{aw(g)}$	0.17
7	$k_0$	0.12	$k_0$	0.15
8	$D_{wM(l)}$	0.04	$\beta_w$	0.05
9	$\beta_w$	0.04	$D_{aw(l)}$	0.01
10	$D_{aw(l)}$	0.01	$D_{wM(l)}$	$3.54 \times 10^{-3}$
11	$D_{aM(l)}$	$3.66 \times 10^{-3}$	$D_{aM(l)}$	$2.32 \times 10^{-3}$
12	$D_{aM(g)}$	$1.40 \times 10^{-3}$	$A_{ha}$	$2.77 \times 10^{-3}$
13	$D_{wM(g)}$	$1.27 \times 10^{-3}$	$D_{aM(g)}$	$1.24 \times 10^{-4}$
14	$A_{ha}$	$6.89 \times 10^{-4}$	$\alpha_a$	$7.25 \times 10^{-6}$
15	$\alpha_a$	$1.85 \times 10^{-6}$	$D_{wM(g)}$	$2.93 \times 10^{-6}$

<sup>a</sup>The sensitivity values represent the overall contribution of each selected parameter to the model output.

The most sensitive parameters under both rh conditions appear to be the parameters of the water–solid interaction energy function and fluid–fluid interaction ( $\kappa$ ). Higher sensitivity values indicate that the estimations of the corresponding parameters from the water uptake data are more reliable, compared to the less sensitive parameters. Very low sensitivity values of the air–solid interaction functions and some matrix diffusivity coefficients, especially under a gaseous state, indicate that these parameters and processes may be neglected for the tested experimental system. However, low sensitivity values do not always necessarily mean an unimportant parameter. For instance, although  $D_{aw(g)}$  appears less sensitive than some parameters, the diffusion is a very important process under the experimental conditions as water vapor transport occurs into the rock sample through a diffusion process from the inlet boundary. Also, the viscous resistance terms,  $k_0$  and  $\lambda$ , do not appear to have large overall sensitivity contributions to water uptake, but as demonstrated below, they have a significant impact on the kinetics of water transport under different rh conditions. The effects of the parameters are further discussed below.

To represent fluid-dependent effects and variation of the fluid–solid interaction forces with the water concentration (see Methods), this study introduced an empirical expression for the intrinsic permeability with its parameters obtained from the experimental data. However, the estimated maximum permeability  $k_0$  (Table 2) is notably low, close to the lower bound of reported values for similar rocks in the literature.<sup>(57)</sup> The suggested form of the permeability model (Figure 3a) represents an overall lower effective permeability during water uptake at low rh conditions and a relatively higher permeability at high rh conditions. While selecting a constant very low permeability ( $<10^{-22}$  m<sup>2</sup>) can represent a transient water uptake at low rh, the same constant value would not work at high rh. The simulations with the higher values of permeability show that water uptake occurs quite rapidly, reaching equilibrium much earlier than the data under both rh conditions (Figure 3c).



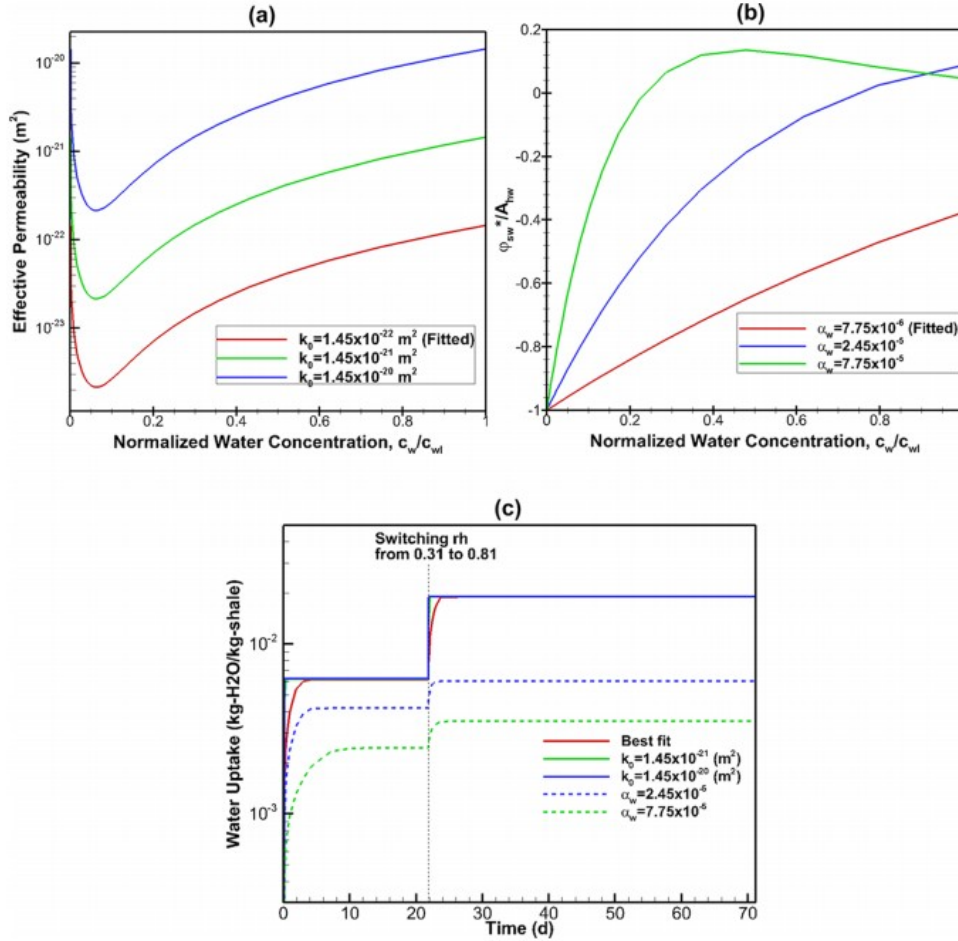


Figure 3. (a) Effective permeability function. (b) Normalized interaction energy. (c) Sensitivity of model-calculated water uptake to permeability and interaction energy parameter changes.

The model-estimated negative values of the fluid–solid interaction term,  $\phi_{sw}^*$ , for the whole range of water concentration (red line in Figure 3b) indicate the existence of a very strong attraction to water molecules within the rock. However, the macroscopic model employed here cannot address the microscopic origin of these interaction forces and the limits of their actions over different length scales of geological nanomaterials. Pore-level application of the classical density functional theory considering molecular interaction forces in detail may be used to explore the individual and collective influences of the surface forces on multicomponent fluid behavior. Experimental measurement of the collective fluid–solid interaction energy is also possible through a water-sorption calorimetry instrument as demonstrated by Drazin and Castro.(58) As shown in Figure 3b, to test the model sensitivity, we varied the  $\alpha_w$  parameter in  $\phi_{sw}^*$  to change the attraction behavior from strongly attractive (best estimate) to partially attractive (blue) and less attractive (green) conditions (Figure 3b). Figure 3c presents the sensitivity of the modeled uptakes to different fluid–solid interaction energy functions. As expected, water uptake decreases considerably with



decreasing magnitude of absolute attraction energy between water and the solid.

The fluid–fluid interfacial force term,  $\kappa$ , is the second most sensitive parameter affecting the modeled water uptakes (Table3). As stated earlier,  $\kappa$  varies with model resolution. The estimated interfacial force term  $\kappa$  is given as a function of the model grid size  $(109 \mu\text{m}/\Delta x)^2$  where  $\Delta x$  is the grid size in micrometers (Table2). The term  $\kappa$  is also one of the least known parameters at macroscopic nanoporous media.  $\kappa$  is related to the interfacial tension between fluids, but systematic pore-scale modeling investigations are needed to characterize the macroscopic  $\kappa$  term with the effects of pore space properties.

Table2 shows that the effective diffusion coefficients in the liquid state appear to be 4–5 orders of magnitude lower than those in the gaseous state. The effective binary diffusion coefficients ( $D_{aw}\tau$ ) under fully saturated gaseous and liquid states are estimated to be  $1.44 \times 10^{-8}$  and  $2.45 \times 10^{-12}$   $\text{m}^2/\text{s}$ , respectively. In the gaseous state, the effective binary diffusion coefficient is similar in magnitude to the effective matrix diffusion coefficients for water and air. The estimated effective matrix diffusion coefficient for water is an order of magnitude lower than the binary diffusion and the matrix diffusion for air. The lower diffusivity for water compared to air might be a result of stronger attraction to water molecules in the rock pore space. The magnitudes of the estimated diffusion coefficients are overall in agreement with reported values for similar rocks.(9,14,59) However, as shown by the sensitivity analysis results in Table3, the low sensitivity values indicate that the estimation of the matrix diffusivity parameters from the water uptake data only may not be precise for the tested experimental conditions.

#### Model-Estimated Concentration Profiles

Under the  $rh = 0.31$  boundary condition, the model produces a water concentration profile in the core sample that represents a diffusion-type behavior with relatively smooth concentration changes through the length of the core (Figure 4a). After increasing  $rh$  to 0.81, the model-produced concentration profiles present a characteristic of immiscible displacement in porous media where a steep gradient of water concentration occurs near the moving front (Figure 5a). Figure 5a demonstrates that the condensation starts to occur near the inlet and induces imbibition into the rock space. The simulated change of water migration patterns when the sample is exposed to a higher  $rh$  is similar to the results obtained by Vincent et al.(18) in a mesoporous medium with pore radii of 1.5–2 nm. In agreement with Vincent et al.,(18) our model results also show a more rapid equilibration of water concentrations during the imbibition-like flow compared to that predicted for diffusion-like transport at lower  $rh$ . However, as mentioned before, the experimental data from the Marcellus shale rock did not indicate reaching a definite gravimetric equilibrium at  $rh = 0.81$  because of slow mass increases.

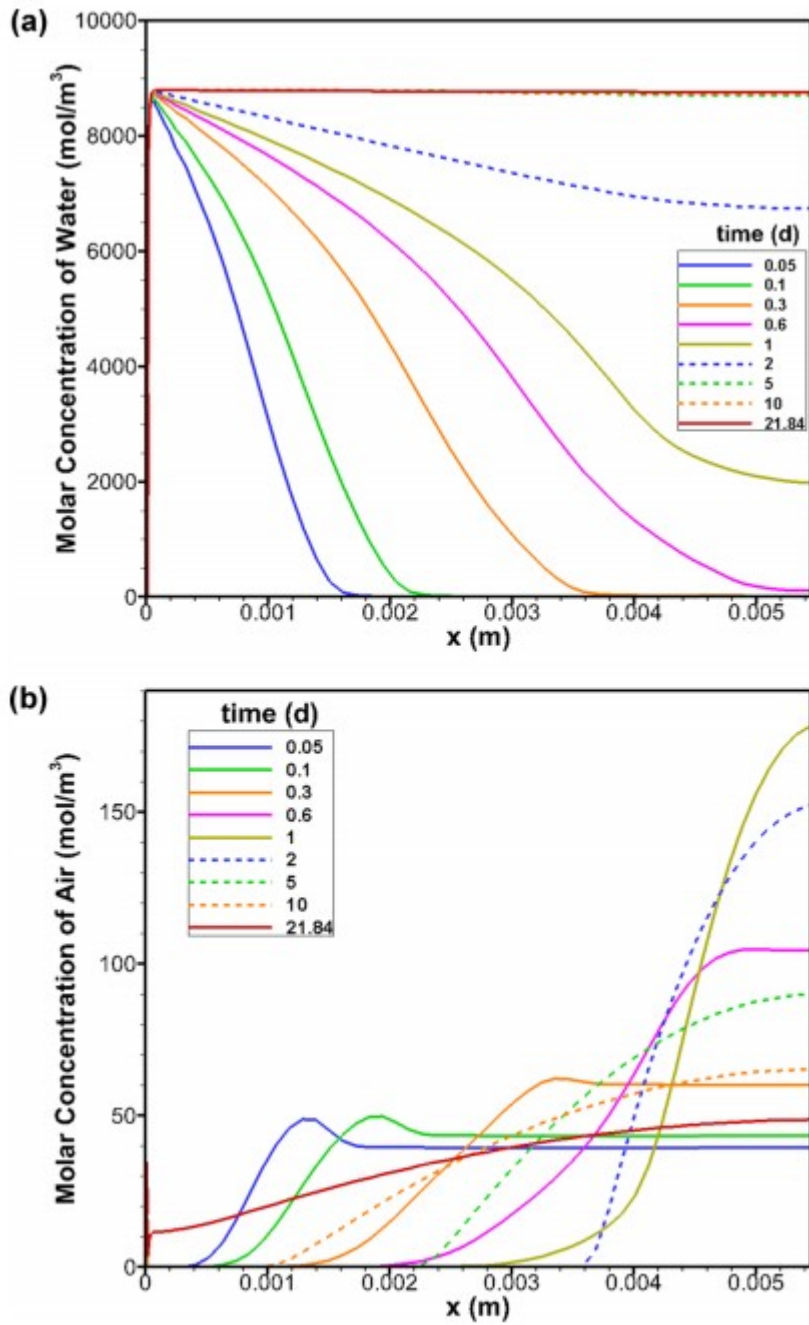


Figure 4. Molar concentration profiles of (a) water and (b) air as functions of time in the shale core at  $rh = 0.31$ .

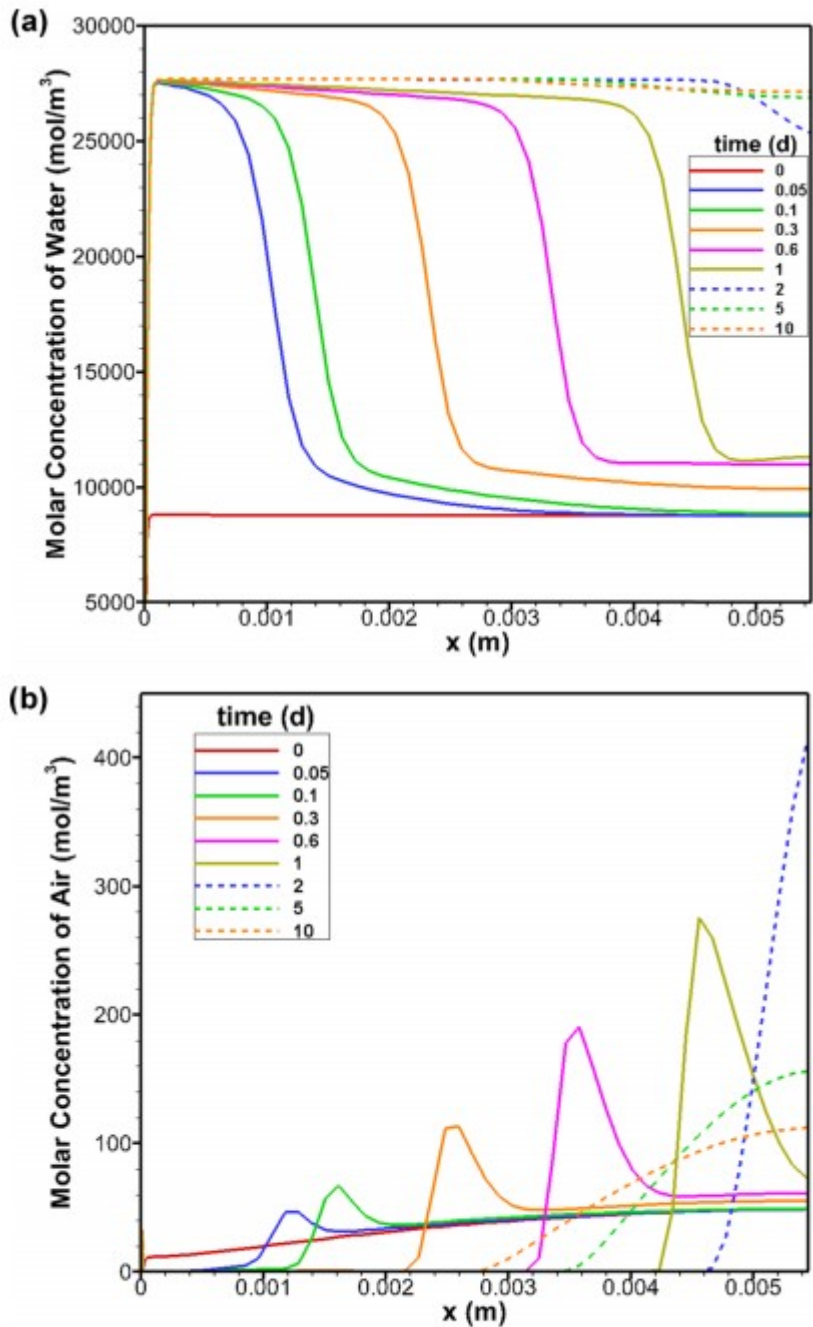


Figure 5. Molar concentration profiles of (a) water and (b) air as functions of time in the shale core after switching  $rh$  from 0.31 to 0.81.

According to the model results, air appears to be moving toward the center of the core ahead of water for the first few days of water vapor uptake at both  $rh = 0.31$  and  $rh = 0.81$  (Figures 4b and 5b). Later, air starts to slowly migrate back toward the inlet, countercurrent to the water flow. Air-solid molecular interaction appears to be negligible compared to the water-solid interaction as can be inferred from comparing the estimated interaction

energy parameters,  $A_{ha}$  and  $A_{hw}$ , in Table 2. However, the model also suggests that the presence of air slows down water migration in the rock. During uptake at  $rh = 0.81$ , the model results show strongly rising air concentrations ahead of the imbibition front, which indicates gas pressurization (Figure 5b). Similar gas pressurization due to the liquid flow in nanoslits was observed experimentally in earlier studies.(5)

### Influence of Forces

The macroscopic forces acting on the two-phase fluid mixture in the nanoporous medium include viscosity and thermodynamic pressure forces as well as the interfacial force between the liquid and gas and the surface force due to fluid-pore wall molecular interactions. Individual forces in terms of force per unit volume are described below.

The viscous resistance force in the porous medium is expressed using a linear drag law based on the Darcy equation as

$$F_{v,x} = -\frac{\mu q_x}{k} \quad (10)$$

The thermodynamic pressure force is a macroscopic manifestation of molecular interaction forces within each fluid phases, expressed by

$$F_{p,x} = -\frac{1}{V} \frac{dP}{dx} \quad (11)$$

The interfacial force between the different phases, which becomes significant along the macroscopic interface of different fluid phases, is expressed by

$$F_{i,x} = \frac{1}{V} \frac{d\sigma}{dx} \quad (12)$$

Finally, the surface force results from molecular interaction forces between fluids and pore walls. The total surface force for an air-water-solid system is defined as

$$F_{s,x} = \frac{1}{V} \frac{dF_s}{dx} \quad (13)$$

The above individual forces were evaluated using the numerical model results fitted to the data. All forces were normalized by the maximum value of the surface force. The surface force, dominated by the interactions between water and the solid, is the main driving force for water migration inside the rock. The maximum value of  $F_{fs}$  at the lower  $rh$  value was selected for normalization to be able to assess the differences between  $rh = 0.31$  and  $rh = 0.81$  conditions. Figure 6 gives the time-dependent changes of the forces at a fixed location ( $x = 2.725$  mm) between the inlet and the center of the core. Negative values of a force in Figure 6 indicate that the corresponding force acts in the  $-x$  direction, toward the inlet and vice versa. Note that the negative and positive force values are always balanced. In

Figure 6a, for the  $rh = 0.31$  test, the magnitude of the normalized forces starts to increase as the diffusive front approaches the fixed  $x$  point. Interfacial forces appear negligible compared to the other forces. The viscous resistance is almost completely balanced with the thermodynamic pressure and the surface forces.

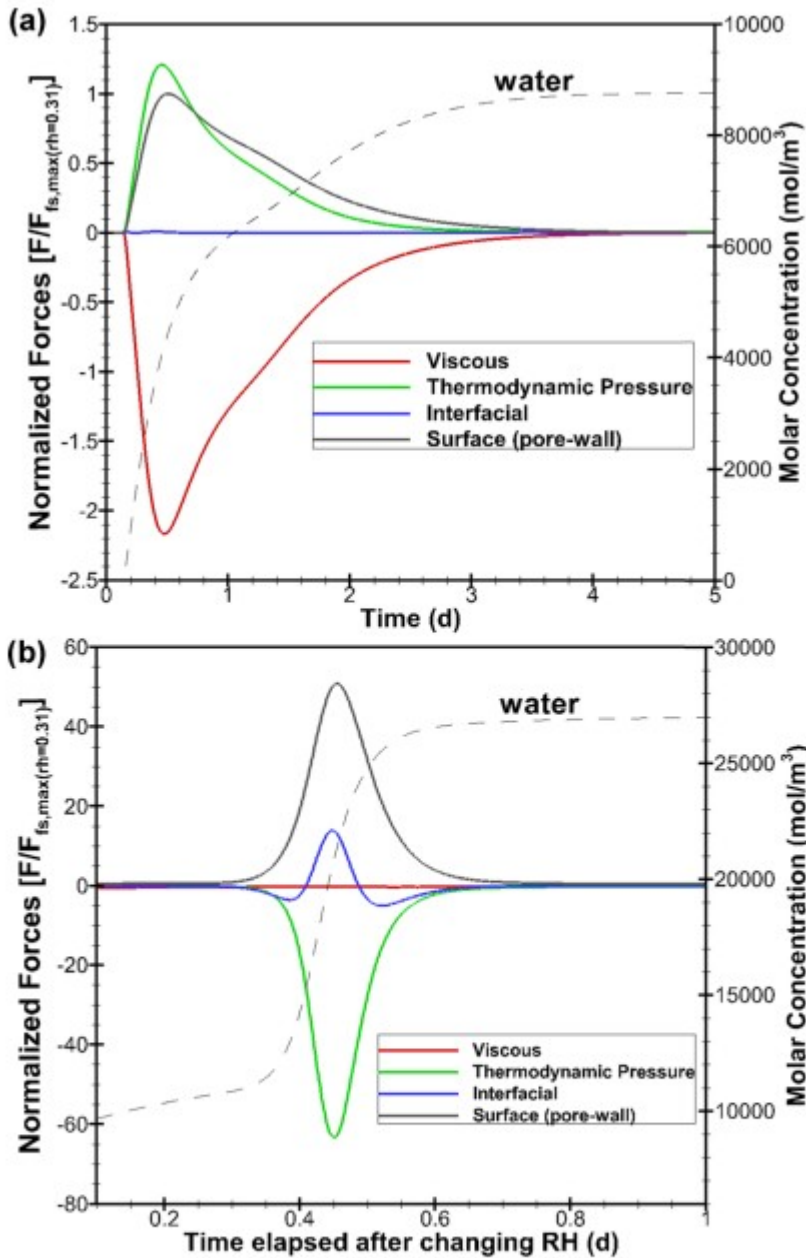


**Figure 6.** Time-dependent contribution of individual forces on fluid behavior in the shale core (at  $x = 2.725$  mm) for (a)  $rh = 0.31$  and (b)  $rh = 0.81$  conditions.

As shown in Figure 6b, interfacial forces become important for the  $rh = 0.81$  conditions, indicating formation and displacement of a macroscopic liquid-gas interface within the rock void spaces. The peak value of  $F_i$  is reached as the macroscopic interface passes through the fixed location. In contrast to the  $rh = 0.31$  test, viscous forces appear to be negligible compared to the other forces because imbibition in the core is governed by interfacial, surface, and thermodynamic pressure forces (Figure 6b). The surface forces are much stronger during  $rh = 0.81$  as a result of higher spatial gradients of  $\phi_{sw}^*$ , which cause condensation near the inlet and drive imbibition through the core. The peak value of  $F_{fs}$  appears to be about 50 times greater at  $rh = 0.81$  than that at  $rh = 0.31$ . The thermodynamic pressure force is also more significant during  $rh = 0.81$  and its sign is negative. Thermodynamically less stable conditions appear to form ahead of the imbibition front due to sharply rising air molar concentrations (Figure 5b) and related pressurization. As a result, the thermodynamic force acts in the negative  $x$  direction, toward the thermodynamically favorable zone, opposite the direction of the liquid water movement at the fixed distance during  $rh = 0.81$ .

## Conclusions

The model presented in the Theory section of this paper has been applied to investigate processes controlling water vapor uptake in a nanoporous rock core exposed to humid air under different relative humidity conditions. The theoretical analyses imply that strong surface forces due to fluid-pore wall attractions are responsible for the significant water uptake observed in the experiments. Because of the attractive nature of the surface forces between water and solids for the specific nanoporous medium tested, condensation occurs at vapor concentrations well below saturation. This behavior is specific to porous materials with pores approaching nanoscales. At low  $rh$  (0.31), diffusion and adsorption processes control water uptake. At high  $rh$  (0.81), condensation near the inlet induces imbibition, and liquid-like water appears to migrate into the rock, as demonstrated by the simulated concentration profiles. These experimental observations and model predictions are consistent with the results obtained in previously reported studies on nanoporous materials. However, the simulated changes in concentration profiles within the shale core need to be confirmed in future experimental studies.

The estimated permeability of the shale rock, based on calibration against the water uptake data, is notably low. Our study points to the need for better understanding fluid dependency effects on transport parameters in nanoconfined pore spaces of the shale rock, including not only permeability but also diffusivity and viscosity. Our theoretical analyses suggest that the surface, interfacial, and thermodynamic pressure forces are the dominant forces acting on fluids during imbibition in nanoporous media. However, further experimental studies are needed to verify our theoretical interpretation of the interaction forces in nanoporous media with complex pore networks.

The experimental data in this study show that the mass in the core sample continues to increase very slowly during the  $rh = 0.81$  experiment without reaching a definite equilibrium. The model used in this study did not reproduce the continued slow mass increase. Our future work will investigate possible effects of chemical reactions. The proposed modeling approach in this study should be extended to accommodate representations of chemical reactions between multiple fluid components and heterogeneous solid phases.

### Acknowledgments

This material is based upon work supported by the U.S. Department of Energy, Office of Fossil Energy, Office of Natural Gas and Petroleum Technology through the National Energy Technology Laboratory (NETL) under award nos. DE-AC02-05CH11231 and FWP-ESD14085. Project management by Stephen Henry (NETL) is gratefully acknowledged. We thank the Marcellus Shale Energy and Environmental Laboratory for the Marcellus Shale samples.

### References

- (1) Alexander, T.; Baihly, J.; Boyer, C.; Clark, B.; Waters, G.; Jochen, V.; Le Calvez, J.; Lewis, R.; Miller, C. K.; Thaeler, J.; Toelle, B. E. Shale gas revolution. *Oilfield Rev.* 2011, 23, 40–55.
- (2) Falk, K.; Coasne, B.; Pellenq, R.; Ulm, F. J.; Bocquet, L. Subcontinuum mass transport of condensed hydrocarbons in nanoporous media. *Nat. Commun.* 2015, 6, 6949.
- (3) Singh, H. A critical review of water uptake by shales. *J. Nat. Gas Sci. Eng.* 2016, 34, 751–766.
- (4) Gelb, L. D.; Gubbins, K. E.; Radhakrishnan, R.; SliwiskaBartkowiak, M. Phase separation in confined systems. *Rep. Prog. Phys.* 1999, 62, 1573.
- (5) Chauvet, F.; Geoffroy, S.; Hamoumi, A.; Prat, M.; Joseph, P. Roles of gas in capillary filling of nanoslits. *Soft Matter* 2012, 8, 10738.
- (6) Franceschini, L.; Soskine, M.; Biesemans, A.; Maglia, G. A nanopore machine promotes the vectorial transport of DNA across membranes. *Nat. Commun.* 2013, 4, 2415.
- (7) Stroock, A. D.; Pagay, V. V.; Zwieniecki, M. A.; Holbrook, N. M. The Physicochemical hydrodynamics of vascular plants. *Annu. Rev. Fluid Mech.* 2014, 46, 615–642.
- (8) Seeman, T.; Bertier, P.; Krooss, B. M.; Stanjek, H. Water vapor sorption on mudrocks. in *Geomechanical and Petrophysical Properties of Mudrocks*; Edited by Rutter, E. H.; et al., Geological Society of London: London, 2017; 201–233.
- (9) Tokunaga, T. K.; Shen, W.; Wan, J.; Kim, Y.; Cihan, A.; Zhang, Y.; Finsterle, S. Water saturation relations and their diffusion-limited equilibration in gas shale: Implications for gas flow in unconventional reservoirs. *Water Resour. Res.* 2017, 53, 9757–9770.
- (10) Barsotti, E.; Tan, S. P.; Saraji, S.; Piri, M.; Chen, J.-H. A review on capillary condensation in nanoporous media: Implications for hydrocarbon recovery from tight reservoirs. *Fuel* 2016, 184, 344–361.
- (11) Gubbins, K. E.; Long, Y.; Sliwiska-Bartkowiak, M. Thermodynamics of confined nano-phases. *J. Chem. Thermodyn.* 2014, 74, 169–183.
- (12) Li, L.; Kazoe, Y.; Mawatari, K.; Sugii, Y.; Kitamori, T. Viscosity

and wetting property of water confined in extended nanospace simultaneously measured from highly-pressurized meniscus motion. *J. Phys. Chem. Lett.* 2012, 3, 2447–2452. (13) Velasco, R.; Pathak, M.; Panja, P.; Deo, M. What happens to permeability at the nanoscale? A molecular dynamics simulation study. *Unconventional Resources Technology Conference 2017*. doi: DOI: 10.15530/URTEC-2017-2697415 (14) Zhang, Y.; Mostaghimi, P.; Fogden, A.; Middleton, J.; Sheppard, A.; Armstrong, R. T. Local diffusion coefficient measurements in shale using dynamic microcomputed tomography. *Fuel* 2017, 207, 312–322. (15) Berthonneau, J.; Obliger, A.; Valdenaire, P. L.; Grauby, O.; Ferry, D.; Chaudanson, D.; Levitz, P.; Kim, J. J.; Ulm, F. J.; Pellenq, R. J.-M. Mesoscale structure, mechanics, and transport properties of source rocks' organic pore networks. *Proc. Natl. Acad. Sci. U. S. A.* 2018, 115, 12365–12370. (16) Bertonecello, A.; Wallace, J.; Blyton, C.; Honarpour, M. M.; Kabir, C. S. Imbibition and water blockage in unconventional reservoirs: Well-management implications during Flowback and early production. *SPE Reservoir Eval. Eng.* 2014, 17, 497–506. (17) Chen, J.; Mehmani, A.; Li, B.; Georgi, D.; Jin, G. Estimation of total hydrocarbon in the presence of capillary condensation for unconventional shale reservoirs. In: *SPE Middle East Oil and Gas Show and Conference. Manama (Bahrain): Society of Petroleum Engineers 2013*, 1–10. (18) Vincent, O.; Marguet, B.; Stroock, A. D. Imbibition triggered by capillary condensation in nanopores. *Langmuir* 2017, 33, 1655–1661. (19) Zhong, J.; Riordon, J.; Zandavi, S. H.; Xu, Y.; Persad, A. H.; Mostowfi, F.; Sinton, D. Capillary condensation in 8 nm deep channels. *J. Phys. Chem. Lett.* 2018, 9, 497–503. (20) Dehghanpour, H.; Zubair, H. A.; Chhabra, A.; Ullah, A. Liquid Intake of organic shales. *Energy Fuels* 2012, 26, 5750–5758. (21) Guo, B.; Ma, L.; Tchelepi, H. A. Image-based micro-continuum model for gas flow in organic-rich shale rock. *Adv. Water Resour.* 2018, 122, 70–84. (22) Saif, T.; Lin, Q.; Bijeljic, B.; Blunt, M. J. Microstructural imaging and characterization of oil shale before and after pyrolysis. *Fuel* 2017, 197, 562–574. (23) Li, Y.; Alibakhshi, M. A.; Zhao, Y.; Duan, C. Exploring ultimate water capillary evaporation in nanoscale conduits. *Nano Lett.* 2017, 17, 4813–4819. (24) van der Waals, J. D. "Thermodynamische theorie der kapillaritat" unter voraussetzung stetiger dichteanderung." *Z. Phys. Chem.* 1894, 13U, 657. (25) Cahn, J.W.; Hilliard, J. E. Free energy of a nonuniform system. I. Interfacial free energy. *J. Chem. Phys.* 1958, 28, 258–267. (26) Hohenberg, P.; Kohn, W. Inhomogeneous electron gas. *Phys. Rev.* 1964, 136, B864–B871. (27) Rowlinson, J. S.; Widom, B. *Molecular theory of capillarity*; Clarendon Press: Oxford, 1982. (28) Evans, R. Fluids adsorbed in narrow pores: phase equilibria and structure. *J. Phys.: Condens. Matter* 1990, 2, 8989. (29) Dinariev, O. Y. A hydrodynamic description of a multicomponent multiphase mixture in narrow pores and thin layer. *J. Appl. Math. Mech.* 1995, 59, 745–752. (30) Armstrong, R. T.; Berg, S.; Dinariev, O.; Evseev, N.; Klemin, D.; Koroteev, D.; Safonov, S. Modeling of pore-scale two-phase phenomena using density functional hydrodynamics. *Transp. Porous Media* 2016, 112, 577. (31) Dinariev, O. Y.; Evseev, N. V. Modeling of nanoscale liquid mixture



transport by density functional hydrodynamics. *Phys. Rev. E* 2017, 95, No. 063307. (32) Cueto-Felgueroso, L.; Fu, X.; Juanes, R. Pore-scale modeling of phase change in porous media. *Phys. Rev. Fluids* 2018, 3, No. 084302. (33) Cueto-Felgueroso, L.; Juanes, R. A phase field model of unsaturated flow. *Water Resour. Res.* 2009, 45, W10409. (34) Papatzacos, P. A model for multiphase and multicomponent flow in porous media, built on the Diffuse-Interface assumption. *Transp. Porous Media* 2010, 82, 443–462. (35) Yang, A. J. M.; Fleming, P. D., III; Gibbs, J. H. Molecular theory of surface tension. *J. Chem. Phys.* 1976, 64, 3732. (36) Churaev, N. V. *Liquid and Vapor Flows in Porous Bodies: Surface Phenomena*; CRC press: New York, 2000. (37) Israelachvili, J. N. *Intermolecular and Surface Forces*, 3rd Edition; Elsevier 2011. (38) Ono, S.; Kondo, S. *Molecular Theory of Surface Tension in Liquids. Structure of Liquids/Struktur der Flüssigkeiten*; Handbuch der Physik; Springer, 1960; 10, 134–280. (39) Krishna, R.; Wesselingh, J. A. The Maxwell-Stefan approach to mass transfer. *Chem. Eng. Sci.* 1997, 52, 861–911. (40) Vignes, A. Diffusion in binary Solutions. Variation of Diffusion Coefficient with Composition. *Ind. Eng. Chem. Fundam.* 1966, 5, 189–199. (41) Krishna, R. Multicomponent surface diffusion of adsorbed species: A description based on the generalized Maxwell-Stefan equations. *Chem. Eng. Sci.* 1990, 45, 1779–1791. (42) Papatzacos, P. A model for multiphase, multicomponent and thermal flow in neutrally wetting porous media, built on the diffuseinterface assumption. *J. Pet. Sci. Eng.* 2016, 143, 141–157. (43) Wise, D. L.; Houghton, G. The diffusion coefficients of ten slightly soluble gases in water at 10–60°C. *Chem. Eng. Sci.* 1966, 21, 999–1010. (44) Walton, J. P. R. B.; Quirke, N. Capillary condensation: A molecular simulation study. *Mol. Simul.* 1989, 2, 361–391. (45) Sarkisov, L.; Monson, P. A. Modeling of adsorption and desorption in pores of simple geometry using molecular dynamics. *Langmuir* 2001, 17, 7600–7604. (46) Chalmers, G. R.; Bustin, R. M.; Power, I. M. Characterization of gas shale pore systems by porosimetry, pycnometry, surface area, and field emission scanning electron microscopy/transmission electron microscopy image analyses: Examples from the Barnett, Woodford, Haynesville, Marcellus, and Doig units. *AAPG Bull.* 2012, 96, 1099–1119. (47) Clarkson, C. R.; Solano, N.; Bustin, R. M.; Bustin, A. M. M.; Chalmers, G. R. L.; He, L.; Melnichenko, Y. B.; Radlinski, A. P.; Blach, T. P. Pore structure characterization of North American shale gas reservoirs using USANS/SANS, gas adsorption, and mercury intrusion. *Fuel* 2013, 103, 606–616. (48) Greenspan, L. Humidity fixed-points of binary saturated aqueous solutions. *J. Res. Natl. Bur. Stand., Sect. A* 1977, 81, 89–96. (49) Gelb, J.; Gu, A.; Fong, T.; Hunter, L.; Lau, S.H.; Yun, W. A closer look at shale: Representative elementary volume analysis with laboratory 3D X-ray computed microtomography and nanotomography. *International Symposium of the Society of Core Analysts* 2011, 58, 1–8 (18–21 September). (50) Keller, L. M. On the representative elementary volumes of clay rocks at the mesoscale. *J. Geol. Min. Res.* 2015, 7, 58–64. (51) Saraji, S.; Piri, M. The representative sample size in shale oil rocks and nano-scale characterization of transport properties. *Int. J. Coal Geol.* 2015, 146, 42–54.

(52) Jerz, J. K.; Rimstidt, J. D. Pyrite oxidation in moist air. *Geochim. Cosmochim. Acta* 2004, 68, 701–714. (53) Hoover, S. E.; Greenawalt, W.; Tittmann, B. Experimental and theoretical modeling of expansion in pyritic shale. *Geotech. Test. J.* 2015, 38, 166–178. (54) Price, K.; Storn, R.; Lampinen, J. *Differential Evolution: A Practical Approach to Global Optimization*; Springer: Berlin, Germany, 2005. (55) Cihan, A.; Birkholzer, J.; Trevisan, L.; Gonzalez-Nicolas, A.; Illangasekare, T. Investigation of representing hysteresis in macroscopic models of two-phase flow in porous media using intermediate scale experimental data. *Water Resour. Res.* 2017, 53, 199–221. (56) Cihan, A.; Birkholzer, J. T.; Bianchi, M. Optimal well placement and brine extraction for pressure management during CO<sub>2</sub> sequestration. *Int. J. Greenhouse Gas Control* 2015, 42, 175–187. (57) Neuzil, C. E. How permeable are clays and shales? *Water Resour. Res.* 1994, 30, 145–150. (58) Drazin, J.W.; Castro, R. H. R. Water adsorption microcalorimetry model: Deciphering surface energies and water chemical potentials of nanocrystalline oxides. *J. Phys. Chem. C* 2014, 118, 10131–10142. (59) Peng, S.; Hu, Q.; Hamamoto, S. Diffusivity of rocks: Gas diffusion measurements and correlation to porosity and pore size distribution. *Water Resour. Res.* 2012, 48, W02507.